

JADES: Nitrogen Enhancement in High-Redshift Broad-Line Active Galactic Nuclei

Yuki Isobe,^{1,2,3*} Roberto Maiolino,^{1,2,4} Francesco D’Eugenio,^{1,2} Mirko Curti,⁵ Xihan Ji,^{1,2} Ignas Juodžbalis,^{1,2} Jan Scholtz,^{1,2} Anne Feltre,⁶ Stéphane Charlot,⁷ Hannah Übler,⁸ Andrew J. Bunker,⁹ Stefano Carniani,¹⁰ Emma Curtis-Lake,¹¹ Zhiyuan Ji,¹² Nimisha Kumari,¹³ Pierluigi Rinaldi,¹² Brant Robertson,¹⁴ Chris Willott,¹⁵ and Joris Witstok^{16,17}

¹Kavli Institute for Cosmology, University of Cambridge, Madingley Road, Cambridge, CB3 0HA, UK

²Cavendish Laboratory, University of Cambridge, 19 JJ Thomson Avenue, Cambridge, CB3 0HE, UK

³Waseda Research Institute for Science and Engineering, Faculty of Science and Engineering, Waseda University, 3-4-1, Okubo, Shinjuku, Tokyo 169-8555, Japan

⁴Department of Physics and Astronomy, University College London, Gower Street, London WC1E 6BT, UK

⁵European Southern Observatory, Karl-Schwarzschild-Strasse 2, 85748 Garching, Germany

⁶INAF-Osservatorio Astrofisico di Arcetri, Largo E. Fermi 5, 50125 Firenze, Italy

⁷Sorbonne Université, CNRS, UMR 7095, Institut d’Astrophysique de Paris, 98 bis bd Arago, 75014 Paris, France

⁸Max-Planck-Institut für extraterrestrische Physik (MPE), Gießenbachstraße 1, 85748 Garching, Germany

⁹Department of Physics, University of Oxford, Denys Wilkinson Building, Keble Road, Oxford OX1 3RH, UK

¹⁰Scuola Normale Superiore, Piazza dei Cavalieri 7, I-56126 Pisa, Italy

¹¹Centre for Astrophysics Research, Department of Physics, Astronomy and Mathematics, University of Hertfordshire, Hatfield AL10 9AB, UK

¹²Steward Observatory, University of Arizona, 933 North Cherry Avenue, Tucson, AZ 85721, USA

¹³AURA for European Space Agency, Space Telescope Science Institute, 3700 San Martin Drive, Baltimore, MD, 21210, USA

¹⁴Department of Astronomy and Astrophysics University of California, Santa Cruz, 1156 High Street, Santa Cruz CA 96054, USA

¹⁵NRC Herzberg, 5071 West Saanich Rd, Victoria, BC V9E 2E7, Canada

¹⁶Cosmic Dawn Center (DAWN), Copenhagen, Denmark

¹⁷Niels Bohr Institute, University of Copenhagen, Jagtvej 128, DK-2200, Copenhagen, Denmark

Accepted 2025 May 14. Received 2025 May 09; in original form 2025 February 17

ABSTRACT

The unexpectedly high nitrogen-to-oxygen (N/O) ratios observed in high-redshift (z) galaxies have challenged our understanding of early star formation. Notably, many of these nitrogen-rich galaxies show signatures of active galactic nuclei (AGNs), suggesting a possible connection between black hole formation and nitrogen enrichment. To explore this connection, we analyse stacked spectra of $z = 4 - 7$ broad-line and narrow-line AGNs using deep NIRSpec data from the JADES survey. We identify a significant N III quintuplet and a high electron density ($\sim 10^4 \text{ cm}^{-3}$) only in the broad-line AGN stack, indicating nitrogen-rich ($\log(\text{N}/\text{C}) \simeq 0.5$, $\log(\text{N}/\text{O}) > -0.6$) and dense gas similar to the high- z nitrogen-rich galaxies. Our findings suggest that dense nuclear star formation may trap nitrogen-rich gas in proto-globular clusters, in line with the high N/O observed in local globular clusters; associated runaway stellar collisions could produce intermediate-mass black hole seeds, as predicted by some models and simulations, whose accretion results into AGN signatures. These findings support scenarios connecting the early black hole seeding and growth to merging processes within and between proto-globular clusters in primeval galaxies.

Key words: galaxies: high-redshift – ISM: abundances – galaxies: active – galaxies: star formation

1 INTRODUCTION

Chemical abundance ratios of the galaxy interstellar medium, such as nitrogen-to-oxygen (N/O), trace accumulated yields of dying stars with varying masses, serving as key indicators of star formation history. Observations (e.g., Izotov et al. 2006) and models (Vincenzo et al. 2016) show that N/O generally increases with gas-phase metallicity (O/H): primary nitrogen (N) production by massive stars with predominant oxygen (O) from core-collapse supernovae (CCSNe) during $12 + \log(\text{O}/\text{H}) \lesssim 8.2$, secondary N production from asymp-

totic giant branch (AGB) stars during $12 + \log(\text{O}/\text{H}) \sim 8.2 - 8.6$, and the galactic wind removing O during $12 + \log(\text{O}/\text{H}) \gtrsim 8.6$. Although the N/O value has a large scatter at $12 + \log(\text{O}/\text{H}) \sim 7.6 - 8.3$ (Kumari et al. 2018) possibly due to Wolf-Rayet (WR) stars (e.g., Kumari et al. 2018) or metal-poor inflow (e.g., Amorín et al. 2010), their N/O values rarely exceed the solar abundance (cf. Mrk996; Telles et al. 2014).

However, the *James Webb Space Telescope* (JWST; Gardner et al. 2023; Rigby et al. 2023) has identified ~ 10 galaxies with super-solar N/O ratios at $z \gtrsim 5$ (e.g., Bunker et al. 2023; Ji et al. 2024; Schaerer et al. 2024). These galaxies are also N-rich with respect to carbon (C), indicative of CNO-cycle processed gas (Isobe et al.

* E-mail: yi264@cam.ac.uk (YI)

2023b, see also Arellano-Córdova et al. 2024). Notably, many of these N-rich galaxies have high electron densities n_e (e.g., Yanagisawa et al. 2024; Topping et al. 2025), high stellar mass surface densities (e.g., Schaerer et al. 2024), and/or compact morphology (Harikane et al. 2025). From these facts, the possibility that nitrogen is enriched in dense starbursts has been actively discussed (e.g., Topping et al. 2025). This might also suggest the link between N-rich galaxies and proto-globular clusters (GCs; e.g., Senchyna et al. 2024; Renzini 2023; D’Antona et al. 2023).

It is also worth mentioning that about half of the N-rich galaxies are reported to have signatures of active galactic nuclei (AGNs), such as broad-line regions (BLRs) for GS_3073 (Übler et al. 2023; Ji et al. 2024), CEERS_01019 (Larson et al. 2023), and CANUCS-LRD-z8.6 (Tripodi et al. 2024), ultra-dense gas for GN-z11 (Maiolino et al. 2024a; but see also Álvarez-Márquez et al. 2025), [Ne v] λ 3426 for JADES-GS-z9-0 (Curti et al. 2024), and X-rays in GHZ9 (Napolitano et al. 2024). Therefore, there might be a connection between N-enrichment, proto-GC formation, and AGN activity. Indeed, runaway mergers inside star clusters are thought to be a major path to provide massive black hole (BH) seeds (e.g., Inayoshi et al. 2020; Partmann et al. 2025; Rantala et al. 2024a).

JWST has discovered many AGN candidates at high z (e.g., Kocevski et al. 2023; Harikane et al. 2023; Maiolino et al. 2024b; Taylor et al. 2024; Mazzolari et al. 2024), allowing us to verify whether high- z AGNs are N-rich. Although most of these AGNs are not bright enough to produce observable N lines, it may be possible to detect them by stacking available spectra.

In this Letter, we report the CNO abundances of high- z AGNs using their stacked spectra observed with the JWST/Near Infrared Spectrograph (NIRSpec; Böker et al. 2022; Jakobsen et al. 2022). We explain our data and sample in Section 2, analysis in Section 3, results and discussions in Section 4, and conclusions in 5. Throughout this Letter, we refer to He II λ 1640 as He II, O III λ 1661,1666 as O III, N III λ 1747-1754 as N III, C III λ 1907,1909 as C III, and [O II] λ 3727,3729 as [O II] for simplicity. Throughout this Letter, we use the solar abundance ratios of Asplund et al. (2021).

2 DATA AND SAMPLE

We analyse the data obtained by the JWST Advanced Deep Extragalactic Survey (JADES; Bunker et al. 2020; Rieke 2020; Eisenstein et al. 2023a), using the JWST/NIRSpec micro-shutter array (MSA; Jakobsen et al. 2022; Ferruit et al. 2022). JADES consists of six programmes (PIDs 1180, 1181, 1210, 1286, 1287, and 3215) in GOODS-S and GOODS-N. In this Letter, we use the JADES data processed by November 2024, which include complete datasets of the four programmes (PIDs 1180, 1181, 1210, and 3215 – see Bunker et al. 2024; D’Eugenio et al. 2025; Eisenstein et al. 2023b) and part of the two programmes (PIDs 1286 and 1287). The JADES has NIRSpec data with $R \sim 100$ and $R \sim 1000$ (R100 and R1000, hereafter) covering $\sim 1\text{--}5\ \mu\text{m}$, which we use in this Letter.

The observed JADES data were reduced by the NIRSpec GTO Team, using the data reduction pipeline developed by the ESA NIRSpec Science Operations Team (Ferruit et al. 2022) and the NIRSpec GTO Team (Alves de Oliveira et al. 2018), whose details are presented in D’Eugenio et al. (2025). Our 1D spectra are a re-extraction of the JADES data. Our main targets are high- z AGNs, which should be compact. To increase the S/N in the blue regions of the spectrum where the JWST point spread function is narrowest, we adopt a 3-pixel box-car aperture (instead of the standard 5-pixel aperture presented in D’Eugenio et al. 2025). The standard pipeline uses

error propagation, with variance-conserving resampling to (conservatively) account for correlated noise (Dorner et al. 2016). We also use spectra whose z values are reliably determined from multiple emission lines (i.e., flag values of 6, 7, or 8; D’Eugenio et al. 2025).

We use a sample of broad-line AGNs (aka Type-1 AGNs), which are selected by Juodžbalis et al. (2025) using the full JADES NIRSpec data based on a broad-component detection ($S/N > 5$) in H α (cf. Juodžbalis et al. 2024). These H α -selected Type-1 AGNs are located at $z < 7$ due to the wavelength coverage of NIRSpec. We focus on $z > 4$, where the R100 spectra fully cover key emission lines of N III, O III, and C III. This Letter targets all these Type-1 AGNs at $z = 4\text{--}7$, whose number is twenty.

We also construct a “Type-2 AGN” sample using Type-2 AGN candidates, which Scholtz et al. (2023) selected from part of the JADES programmes (PIDs 1210 and 3215) based on emission line diagnostics of [N II] λ 6583/H α vs. [O III] λ 5007/H β (Baldwin et al. 1981), [S II] λ 6731/H α vs. [O III] λ 5007/H β (Veilleux & Osterbrock 1987), and those based on high-ionisation lines (e.g., He II; Hirschmann et al. 2023). We use all these Type-2 AGN candidates at $z = 4\text{--}7$, whose number is eighteen. Note that there is only one overlap between our Type-1 and Type-2 AGN samples, which means that most of our Type-2 AGNs are narrow-line AGNs.

Additionally, excluding our Type-1 or Type-2 AGNs, we obtain 665 galaxies at $z = 4\text{--}7$ where no evidence of AGN has been identified. Hereafter, we refer to this galaxy sample as the “Non-AGN” sample. Note that our three samples have similar median z values of 5.2–5.3.

3 ANALYSIS

3.1 Emission Line Fitting for Individual Galaxies

We conduct emission line fitting for individual galaxies to obtain redshifts based on the R100 and R1000 spectra independently. We model the spectra around H β and [O III] λ 4959,5007 with 3 Gaussian functions and a constant continuum level. We use the z values with visual inspection (D’Eugenio et al. 2025) as an initial guess. We fix the ratio of [O III] λ 5007/[O III] λ 4959 to 2.98 (Kojima et al. 2020). We also use the same width for H β and [O III] λ 4959,5007. There are 64 overlaps (2 of Type-1, 12 of Type-2, and 50 of Non-AGN sources) between our sample and Bunker et al. (2024), whose z values based on the R100 data are different by only at most 0.1%. This analysis provides not only the z values but also [O III] λ 5007 fluxes ($F([\text{O III}])$), which are used to normalise the spectra in Section 3.2.

3.2 Stacking

We produce stacked spectra of the R100 and R1000 data in the same manner. We shift the spectra to the restframe and then resample them to a common wavelength grid, for which the spectral pixel size is set to half of the full-width half maximum based on the NIRSpec spectral resolution. We use the spectral resolution in the case of compact/point-like sources (hence smaller than the shutter width; de Graaff et al. 2024), which is generally two times better than the nominal resolution, which applies only to the case of uniformly illuminated shutter. The resampling to the common wavelength grid is done using spectres (Carnall 2017), which also propagates the errors of the individual spectra to those of the resampled spectra.

Finally, we renormalise the resampled spectra by the $F([\text{O III}])$ values obtained in Section 3.1, and then we define the stacked spectrum by taking the median of the normalised spectra without any weighting at each wavelength of the common λ_{rest} grid, which underlies all the

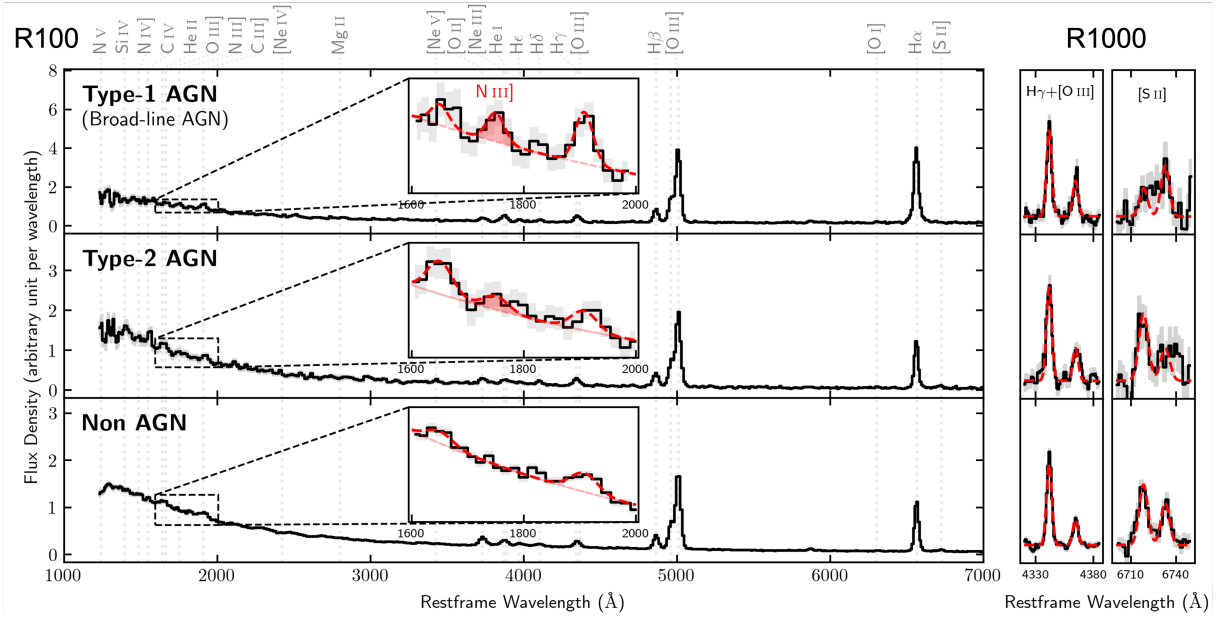


Figure 1. **Left:** R100 composite spectra of the median stacking (black solid line) with the error (gray shade) of the Type-1 AGN (top), the Type-2 AGN (middle), and the Non-AGN samples (bottom). The inset panels show fitting results of the UV emission lines (red dashed curve), highlighting N III lines with the red shade. **Right:** R1000 stacked spectra around H γ + [O III] λ 4363 and [S II]. The symbols are the same as the left figure.

results reported in this Letter. This stacking method helps mitigate the influence of a few bright outliers, ensuring that the resulting spectra more accurately represent the average properties of the individual galaxies. We obtain errors of the stacked spectrum by performing a Monte Carlo simulation. We create 1000 stacked spectra based on the individual spectra randomly fluctuated by their errors under the assumption of the normal distribution, and calculate the standard deviation at each wavelength. When we adopt this method to the mean stacking, it can reproduce the errors propagated from the individual error spectra as done by [Steidel et al. \(2016\)](#). Bootstrap resampling is another method to account for the errors of the stacked spectra. However, we do not use bootstrap errors for emission lines, as they overestimate flux variance by including the strong effect of variation of the underlying continuum emission from source to source. The stacked spectra are shown in Fig. 1.

3.3 Emission Line Measurement

We conduct emission line fitting for the stacked spectra in the following three wavelength regions (UV: 1600–2000, blue: 3600–5200, red: 6200–7300 Å). As the exposure time for the R100 data was generally longer than that for the R1000 data by a factor of 1–4 ([D’Eugenio et al. 2025](#)), we derive key emission line fluxes (He II+O III, N III, C III, [O II], H β , [O III] λ 4495,5007, H α + [N II] λ 6548,6583) using the R100 data, except for [O III] λ 4363/[O III] λ 5007 and [S II] λ 6716/[S II] λ 6731. We obtain these ratios by resolving [O III] λ 4363 from H γ and [S II] λ 6716 from [S II] λ 6731 with the R1000 data in the less noisy restframe optical range. All our Type-1 AGNs have R1000 data, only one of which does not cover [O III] λ 4363, while the others cover both [O III] λ 4363 and [S II]. Also, 95% of our Type-2 and Non-AGNs have R1000 data, 80–90% of which cover [O III] λ 4363 and [S II]. Due to the difficulty of decomposing O III from He II with the R100 spectra, we treat He II+O III as O III, which serves as an upper limit of the O III flux. We also add a broad Gaussian component for the H α of the

Type-1 AGN stack at the same wavelength as the narrow component. At $z = 4 - 7$ with R100 data, the ratio of maximum to minimum resolution is only ~ 1.3 in the rest-frame UV but 2.2–2.4 in the rest-frame optical. However, we find that the cumulative integral of H α in the Non-AGN stack, which excludes Type-1 AGNs, exceeds that from Gaussian fitting by only $\sim 3\%$. This suggests that profile smearing due to resolution differences has a negligible impact on our line flux measurement. We use the same width for the emission lines, and model the continuum with a power law function at each wavelength region. The best-fit widths of the R100 data lie between those of the resolutions for compact/point-like sources and for nominal extended sources. We set a detection criterion of $S/N > 2$, and calculate 2σ upper limits for undetected lines. The inset panels of Fig. 1 highlight the fitting results of the UV wavelength region. We find a detection of 2.6σ (i.e., P value < 0.005) in the Type-1 AGN stack. Note that, since the redshift is fixed, we use the line S/N to infer the significance, with no need to account for the look-elsewhere effect. In contrast, N III is not significantly detected in the Type-2 AGN stack (1.6σ) or the Non-AGN stack (0.0σ). We have checked that this finding holds true regardless of the stacking method (median vs. mean) or normalisation parameter (i.e., $F([O III])$, [O III] luminosity, vs. continuum at restframe 5500–6000 Å). Note that N III lines with $S/N = 2.4$ – 2.6 are seen in 3 out of 20 individual R100 spectra of our Type-1 AGNs. However, even removing these sources, we see a $\sim 2\sigma$ N III in the Type-1 AGN stack, suggestive of the overall nature. Similarly, using the R100 data, we find that 2 out of 18 Type-2 AGNs and ~ 30 out of 665 Non-AGN sources have N III lines with $S/N > 2$. We stress that the absence of N III in our Type-2 and Non-AGN stacks reflects general trends, but does not imply that none of our Type-2 or Non-AGN sources exhibit N III. The observed CNO line ratios of the Type-1 AGN stack ($N III/C III = 0.56 \pm 0.24$ and $N III/O III > 0.99$) are comparable to those of the $z \gtrsim 5$ N-rich galaxies (e.g., [Bunker et al. 2023](#)) and $z \sim 2 - 3$ N-loud quasars ([Batra & Baldwin 2014](#)). Notably, our Type-1 AGN stack does not have C IV, in line with most of the Type-1 AGNs found with the

JWST, which may be due to the optically-thick disc softening the incident spectrum (Lambrides et al. 2024), possibly associated with high accretion rate. Line fluxes are listed in Tab. 1.

3.4 Nebular Properties

We derive the colour excess $E(B - V)$, the electron temperature $T_e(\text{O III})$, and the electron density $n_e(\text{S II})$ as follows. The $E(B - V)$ values are derived from the $\text{H}\beta/\text{H}\alpha$ ratio, whose intrinsic value under the assumptions of the case B recombination is derived with PyNeb (Luridiana et al. 2015). We use the same atomic data as Isobe et al. (2023b) except that we use Lennon & Burke (1994)’s data for the O^{2+} collisional strength. We assume the average SMC extinction curve (Gordon et al. 2003) with $R_V = 3.1$, which is consistent with observations of galaxies at $z \sim 1 - 3$ (Reddy et al. 2023a). For the Type-1 AGN stack, we use the $\text{H}\alpha$ flux value of the narrow component. The obtained $E(B - V)$ values are consistent with those derived from $\text{H}\gamma/\text{H}\beta$ ratios within 1σ , where $\text{H}\gamma$ is decomposed from $[\text{O III}]\lambda 4363$ using the R1000 spectra. The R1000 spectra also indicate that contamination from $[\text{N II}]\lambda 6583$ to $\text{H}\alpha$ would be at most $\sim 3\%$ for all samples (cf. Cameron et al. 2023b; Sandles et al. 2024), which can only reduce the $E(B - V)$ value by $\lesssim 0.03$ and the N/C value by $\lesssim 0.02$ dex, and rather increase the N/O value by $\lesssim 0.01$ dex. We also use PyNeb to derive the $T_e(\text{O III})$ value from the $[\text{O III}]\lambda 4363/[\text{O III}]\lambda 5007$ ratio and the $n_e(\text{S II})$ value from the $[\text{S II}]\lambda 6716/[\text{S II}]\lambda 6731$ ratio. As the $E(B - V)$, $T_e(\text{O III})$, and $n_e(\text{S II})$ values slightly depend on each other, we calculate $E(B - V)$, $T_e(\text{O III})$, and $n_e(\text{S II})$ values iteratively to find their values consistent with each other (Isobe et al. 2022). We find these values in reasonable ranges of $E(B - V) > 0$ mag and $n_e(\text{S II}) = 4 - 50000 \text{ cm}^{-3}$, the last of which is determined where the $[\text{S II}]$ doublet is sensitive to n_e . We calculate errors of these properties from the 1σ errors of the used emission line ratios.

Using the final value of $E(B - V)$, we obtain dust-corrected fluxes of the stacked spectra. We have checked that the $\text{N III}]$ is detected only in the Type-1 AGN stack even when we correct for the dust reddening based on individual $E(B - V)$ values before the stacking.

We derive ion abundance ratios of O^+/H^+ from $[\text{O II}]/\text{H}\beta$, O^{2+}/H^+ from $[\text{O III}]\lambda 5007/\text{H}\beta$, $\text{N}^{2+}/\text{C}^{2+}$ from $\text{N III}]/\text{C III}]$, $\text{N}^{2+}/\text{O}^{2+}$ from $\text{N III}]/\text{O III}]$, and $\text{C}^{2+}/\text{O}^{2+}$ from $\text{C III}]/\text{O III}]$, using $T_e(\text{O III})$ and $n_e(\text{S II})$ for all ion abundance ratios but $T_e(\text{O II})$ for O^+/H^+ , where $T_e(\text{O II})$ is derived from $T_e(\text{O III})$ based on the empirical relation (Garnett 1992). Similar wavelengths of $\text{N III}]$, $\text{C III}]$, and $\text{O III}]$ make their line ratios less sensitive to flux calibration or dust correction, which are conversely critical for e.g., $\text{N III}]/[\text{O III}]\lambda 5007$. We assume $12 + \log(\text{O}/\text{H})$ to be $12 + \log((\text{O}^+ + \text{O}^{2+})/\text{H}^+)$ (e.g., Izotov et al. 2006).

To derive element abundance ratios, we calculate ionisation correction factors (ICFs), which are defined as e.g., $\text{N}/\text{C} = \text{N}^{2+}/\text{C}^{2+} \times \text{ICF}(\text{N}^{2+}/\text{C}^{2+})$. To obtain $\text{ICF}(\text{N}^{2+}/\text{C}^{2+})$, $\text{ICF}(\text{N}^{2+}/\text{O}^{2+})$, and $\text{ICF}(\text{C}^{2+}/\text{O}^{2+})$, we construct photoionisation models based on stellar and AGN ionising spectra using Cloudy (Ferland et al. 2013) and following the procedure of Isobe et al. (2023b). For both photoionisation models, we vary O/H within $-2 \leq [\text{O}/\text{H}] \leq 1$ in 0.25-dex increments and U within $-3.5 \leq \log(U) \leq -0.5$ in 0.25-dex increments. We also assume the hydrogen density n_{H} to be 300 cm^{-3} and He/H and metal-to-oxygen ratios to be the solar abundances. Note that the derived densities are all significantly below the critical densities of lines used for the CNO abundance measurements, which makes the choice of density less important.

To construct stellar photoionisation models, we use BPASS (Stanway & Eldridge 2018) binary stellar spectra under the assumption of an instantaneous star-formation history with the stellar age of 10 Myr

and an upper star mass cut of $100 M_{\odot}$ with the Salpeter (1955) initial mass function (IMF). Different stellar age (1–100 Myr) and upper star mass cut (100 and $300 M_{\odot}$) can change the ICFs by only $\lesssim 0.01$ dex. We also construct AGN photoionisation models assuming the AGN radiation model of Cloudy, whose parameter sets are the big-bump temperature of $T_{\text{BB}} = 1.5 \times 10^5 \text{ K}$, the X-ray to UV ratio of $\alpha_{\text{OX}} = -1.4$, the low-energy slope of the big-bump component of $\alpha_{\text{UV}} = -0.5$, and the X-ray component slope of $\alpha_{\text{X}} = -1.0$.

We choose the model whose metallicity is the closest to the observed value. We make the ICF as a function of $[\text{O III}]\lambda 5007/[\text{O II}]$ by performing a linear interpolation of the ICF values based on the model $[\text{O III}]\lambda 5007/[\text{O II}]$ values. We then obtain the ICF value at the observed $[\text{O III}]\lambda 5007/[\text{O II}]$ value. The obtained ICFs are ≈ 1 (Tab. 2), indicating only a small (< 0.08 dex) correction. The ICFs can also change by only $\lesssim 0.1$ dex when we add dust that causes the observed extinction of $E(B - V) \lesssim 0.4$ mag only within the modelled ionised region, which is an extreme case because the dust optical depth within the ionised gas is usually very low (Bottorff et al. 1998). We also obtain $\log(U)$ values from $[\text{O III}]\lambda 5007/[\text{O II}]$ ratios using the Cloudy models.

We finally obtain element abundance ratios of N/C, N/O, and C/O from the ion abundance ratios and the ICFs. We adopt the ICFs based on the AGN photoionisation models for the Type-1 and Type-2 AGN stacks, and those based on the stellar photoionisation models for the Non-AGN stack. It is worth noting that the derived ICFs are ~ 1 because the used ions have similar ionisation energies. This also leads to comparable values of the ICFs based on the AGN and stellar photoionisation models. We obtain errors of the abundance ratios with a Monte Carlo simulation by repeating the calculation 1000 times based on the flux values randomly perturbed by their errors. The nebular properties are listed in Tab. 2. Note that the Type-1 AGN stack has a supersolar N/O ratio, which holds true regardless of the choice of dust attenuation laws (Gordon et al. 2003 vs. Calzetti et al. 2000) or line ratios ($\text{N III}]/\text{O III}]$ or $\text{N III}]/[\text{O III}]\lambda 5007$).

4 RESULT AND DISCUSSION

The left panels of Fig. 2 show CNO abundances of our stacks and N-rich galaxies at $z \gtrsim 5$, whose N abundances are similarly derived from restframe-UV N lines (see also $[\text{N II}]$ -based reports at $z \sim 4 - 6$; Arellano-Córdova et al. 2024; Stiavelli et al. 2025; Zhang et al. 2025). The Type-1 AGN stack shows high N/C and N/O ratios comparable to those of the N-rich galaxies (e.g., Cameron et al. 2023a) and GC stars (Carretta et al. 2005). On the other hand, the N/C and N/O ratios of the Non-AGN stack are lower than many of the N-rich galaxies.

Interestingly, the right panels of Fig. 2 show that the Type-1 AGN stack with the high N/C and N/O ratios has $n_e \sim 10^4 \text{ cm}^{-3}$. This value is significantly higher than that of the Non-AGN stack and previous n_e measurements at similar redshifts (e.g., Isobe et al. 2023a; Reddy et al. 2023b; Li et al. 2025), and comparable to that of the N-rich galaxies (Übler et al. 2023; Isobe et al. 2023a; Larson et al. 2023) and simulated young massive star clusters, promising progenitors of GCs ($10^3 - 10^5 \text{ cm}^{-3}$; Inoguchi et al. 2024).

The Type-2 AGN stack has relatively unconstrained N/C and N/O values, which are not conclusive enough to discuss its N enhancement. However, it is worth mentioning that its $\text{N III}]$ line is less significant than that of the Type-1 AGN stack and that the n_e value is similarly low to that of the Non-AGN stack.

It is worth comparing our results with the stack of $z \sim 4 - 10$ galaxies (Hayes et al. 2025), who also explored N/O in stacked spectra. We avoid strong conclusions since the uncertainties of their results

Table 1. Emission line fluxes before dust correction based on the R100 spectra normalised by the $H\beta$ flux, except for † from the R1000 spectra. The upper limits are 2σ . ‡ : Narrow component.

Sample	O III]	N III]	C III]	[O II]	$H\beta$	[O III] λ 5007	$H\alpha + [N II]\lambda\lambda 6548, 6583$	[O III] λ 4363/[O III] λ 5007 †	[S II] λ 6716/[S II] λ 6731 †
Type-1 AGN	< 0.25	0.25 ± 0.09	0.44 ± 0.09	0.29 ± 0.03	1.00 ± 0.03	5.44 ± 0.05	$4.41 \pm 0.06^{\ddagger}$	0.030 ± 0.003	0.55 ± 0.20
Type-2 AGN	0.89 ± 0.27	< 0.47	0.53 ± 0.21	0.40 ± 0.06	1.00 ± 0.04	5.56 ± 0.03	2.65 ± 0.04	0.032 ± 0.004	2.09 ± 0.74
Non AGN	0.35 ± 0.09	< 0.17	0.55 ± 0.07	0.64 ± 0.02	1.00 ± 0.01	5.82 ± 0.02	3.20 ± 0.02	0.024 ± 0.001	1.43 ± 0.18

Table 2. Nebular properties. † : Showing a 1σ upper limit because the measured value reaches the low density limit. The other limits are 2σ .

Sample	$E(B - V)$	$T_e (10^4 \text{ K})$	$\log(n_e/\text{cm}^{-3})$	$\log(U)$	$12 + \log(\text{O}/\text{H})$	$\log(\text{N}/\text{C})$	$\text{ICF}(\text{N}^{2+}/\text{C}^{2+})$	$\log(\text{N}/\text{O})$	$\text{ICF}(\text{N}^{2+}/\text{O}^{2+})$	$\log(\text{C}/\text{O})$	$\text{ICF}(\text{C}^{2+}/\text{O}^{2+})$
Type-1 AGN	$0.43^{+0.07}_{-0.07}$	$2.19^{+0.14}_{-0.14}$	$3.94^{+0.76}_{-0.52}$	$-2.23^{+0.05}_{-0.03}$	$7.46^{+0.16}_{-0.06}$	$0.50^{+0.17}_{-0.25}$	$1.141^{+0.014}_{-0.002}$	> -0.58	$1.111^{+0.022}_{-0.017}$	> -1.08	$0.973^{+0.012}_{-0.016}$
Type-2 AGN	$0.00^{+0.08}_{-0.08}$	$1.94^{+0.14}_{-0.13}$	$< 1.98^{\dagger}$	$-2.13^{+0.09}_{-0.04}$	$7.55^{+0.07}_{-0.06}$	< 0.57	$1.154^{+0.015}_{-0.004}$	< -0.71	$1.167^{+0.039}_{-0.026}$	$-1.28^{+0.20}_{-0.27}$	$1.011^{+0.022}_{-0.022}$
Non AGN	$0.13^{+0.03}_{-0.03}$	$1.74^{+0.05}_{-0.05}$	$< 2.41^{\dagger}$	$-2.33^{+0.02}_{-0.02}$	$7.68^{+0.03}_{-0.03}$	< 0.14	$1.064^{+0.001}_{-0.002}$	< -0.84	$1.056^{+0.004}_{-0.004}$	$-0.99^{+0.13}_{-0.12}$	$0.992^{+0.005}_{-0.005}$

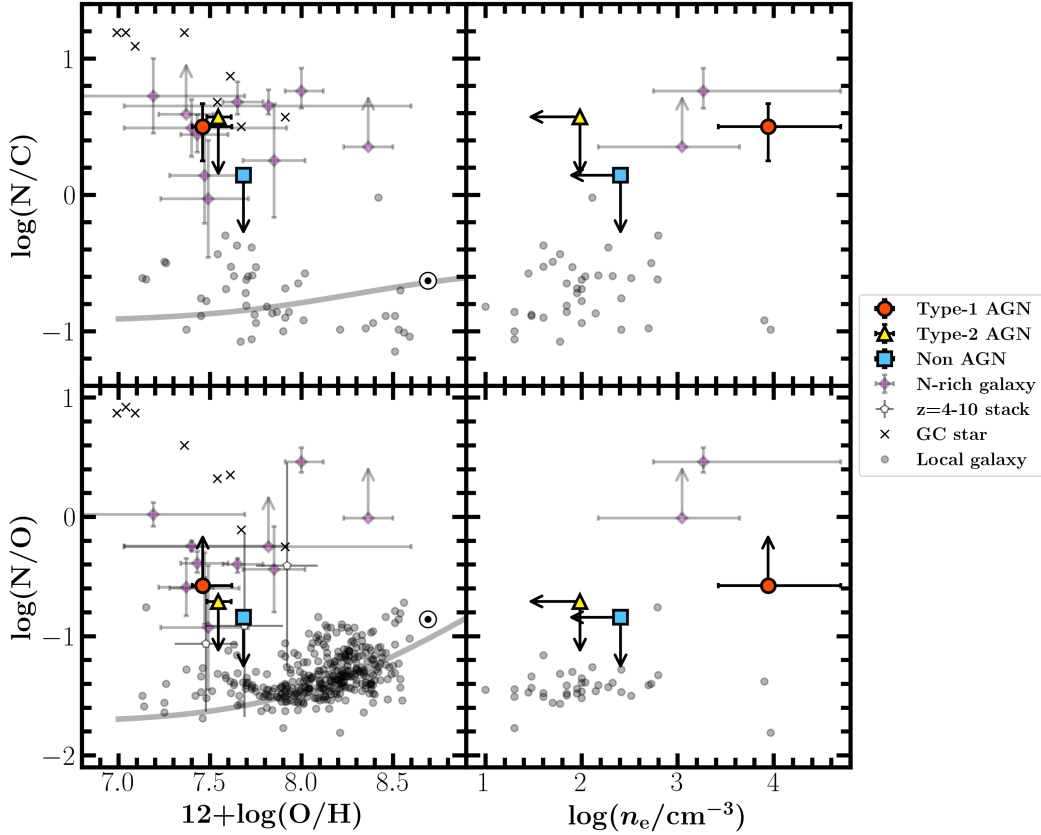


Figure 2. N/C (top) and N/O ratios (bottom) as a function of metallicity, expressed in terms of oxygen abundance O/H (left), and n_e of the singly-ionised region (right). The red circle corresponds to the Type-1 AGN stack, the yellow triangle to the Type-2 AGN stack, the blue square to the Non-AGN stack, the magenta diamonds to the $z \geq 5$ N-rich galaxies (Cameron et al. 2023a; Isobe et al. 2023b; Topping et al. 2024, 2025; Castellano et al. 2024; Ji et al. 2024; Schaerer et al. 2024; Navarro-Carrera et al. 2024; Curti et al. 2024; Napolitano et al. 2024; Übler et al. 2023 and Isobe et al. 2023a for n_e ; see also Senchyna et al. 2024; Marques-Chaves et al. 2024; Larson et al. 2023), the white pentagons to the stack of $z = 4 - 10$ galaxies (Hayes et al. 2025), the black crosses to GC stars (Carretta et al. 2005), the gray dots to local star-forming galaxies (Izotov et al. 2006; Berg et al. 2016; Berg et al. 2019), the gray curve to the empirical relation based on observations of galaxies and Galactic stars (Nicholls et al. 2017), and the circled dot to the solar abundances (Asplund et al. 2021).

are large, but we can say that their measured values are closer to the upper limit of our Non-AGN stack than to the lower limit of our Type-1 AGN stack. This is consistent with the report that Hayes et al. (2025)’s stacked spectra do not show AGN signatures.

What is the origin of the N enhancement in the Type-1 AGN stack? Various contributors have been proposed to explain early N

enhancement, including massive stars ejecting CNO-processed gas via stellar winds (e.g., Watanabe et al. 2024) or tidal disruption events (TDEs; Cameron et al. 2023a), and/or chemically differential winds (e.g., Rizzuti et al. 2024), which may be linked to dense, clustered star formation or supermassive BHs (SMBHs) as in the following evolutionary scenario. Step 1: Dense gas in the nuclear

region of a galaxy could form stars efficiently, which could lead to several star clusters (aka proto-GCs) hosting massive stars or even supermassive stars (SMSs; $\sim 10^3 - 10^5 M_\odot$) through runaway stellar collisions and/or strong gas accretion (e.g., Gieles et al. 2018). N-rich gas can be ejected via stellar winds of massive stars, including SMSs (e.g., Nagele & Umeda 2023; Charbonnel et al. 2023; Nandal et al. 2024), very massive stars ($\sim 10^2 - 10^3 M_\odot$; Vink 2023), and WR stars ($\sim 25 - 120 M_\odot$; e.g., Watanabe et al. 2024; Kobayashi & Ferrara 2024; Fukushima & Yajima 2024). TDEs are also a natural byproduct of high star densities necessary for runaway collisions. Gas accretion can spin up the star, favouring the formation of the WR phase (Dall’Amico et al. 2025). This N-rich gas may be trapped in subsequent generations of stars in the star cluster, which could link to N overabundance of present-day GC stars (e.g., Charbonnel et al. 2023; Pascale et al. 2023). The connection between N enrichment and GCs will also be discussed in detail by Ji et al. (in prep.). Until Step 1), our scenario is similar to that proposed by Topping et al. (2025). We also note that O can easily be expelled from the dense compact region via SN-driven chemically differential winds, which can result in enhancing N/O (Vincenzo et al. 2016; D’Antona et al. 2023; Rizzuti et al. 2024). Step 2): If the stars are massive enough and/or gas accretion is sufficient, the star cluster would develop intermediate-mass BHs (IMBHs) with $\sim 10^3 - 10^4 M_\odot$ (e.g., Rantala et al. 2024b; Partmann et al. 2025). Indeed, observational signatures of IMBHs have also been found in some GCs (e.g., Häberle et al. 2024). IMBHs can also trigger TDEs (e.g., Sakurai et al. 2019). Step 3): Continuous gas accretion onto the IMBH would create a SMBH with a dense accretion disc, providing AGN signatures such as BLRs. The dense accretion disc could also form VMSs (Cantiello et al. 2021), which could contribute to N enrichment. Overall, our observational findings support scenarios in which black hole seeding, and their early growth, is associated with the merging processes within and between proto-GCs in the central regions of primeval galaxies (e.g. Rantala et al. 2024a; Partmann et al. 2025).

Such extreme N enhancement would primarily take place in the central, dense region, possibly the BLR (cf. Maiolino et al. 2024a), but not in the bulk of the host galaxy (see Ji et al. 2024). If such objects are observed from the face-on direction without much obscuration by the dusty torus, N-rich Type-1 AGNs are expected to be seen. Conversely, from the edge-on direction, the dusty torus might hide the N-rich central dense region. This could be the reason why the Type-2 AGN stack does not have a significant N III] detection or a high n_e value. Considering also that the Type-2 AGN stack shows $E(B - V) = 0$ mag, the dust may be strongly localised at the central region. The possibility that some of our Type-2 AGNs might not be AGNs (see Scholtz et al. 2023) would just increase the contribution from the host galaxies, which still fit within our scenario.

Here, we check the CNO abundance measurements of the Type-1 AGN stack, assuming its N III] is emitted from the BLR. The reddening of the BLR is generally greater than that of the narrow-line region (NLR) by $\Delta E(B - V) \lesssim 0.5$ (Heard & Gaskell 2016), which can make the true N/C and N/O values of the Type-1 AGN stack even higher than the observed values by $\lesssim 2$ dex. Although many parameters can affect chemical abundance measurements in the BLR (Temple et al. 2021), we have checked that the BLR photoionisation models of Ji et al. (2024) can slightly reduce the inferred N/C value by ~ 0.2 dex and increase the inferred N/O value by ~ 0.3 dex from the NLR models. Neither case is likely to change our conclusions.

Note that our scenario does not exclude the presence of N-rich galaxies without any AGN signatures. If the star in Step 1) is not massive enough, gas accretion is not sufficient, or the galaxy is too young to reach Step 3), N-rich galaxies would not develop an AGN.

Additionally, high- z AGN may have a short duty cycle, hence they are observable as active only for relatively short periods (Trinca et al. 2024). This can explain some of the high- z N-rich galaxies without AGN signatures such as GLASS_150008 (Isobe et al. 2023b) or A1703-zd6 (Topping et al. 2025). However, it is suggestive that about half of the high- z N-rich galaxies do have AGN signatures. In particular, GS_3073, the galaxy with the highest N/O ratio reported so far at $z \gtrsim 5$ (Ji et al. 2024), is also a luminous Type-1 AGN (Übler et al. 2023), with clearly detected broad permitted line (hence BLR-originated) and coronal lines that rule out photoionisation from stars alone (Ji et al. 2024). Conversely, the fact that we do not detect N III] in the Non-AGN stack indicates that non-AGN galaxies as N-rich as those reported at $z \gtrsim 5$ are a minority in the general galaxy population (while being a majority of the Type-1 AGN population).

5 CONCLUSIONS

Using JWST/NIRSpec data obtained by the JADES survey, we find that the stacked spectrum of Type-1 AGNs at $z = 4 - 7$ shows $\log(N/C) \approx 0.50$, $\log(N/O) > -0.58$, and $n_e \sim 10^4 \text{ cm}^{-3}$, which are higher than those of the Type-2 AGN and Non-AGN stacks and comparable to those of high- z N-rich galaxies. Given that N enhancement is similarly observed in GCs, our findings suggest a close connection between dense proto-GCs and black hole seeding in the early Universe. Specifically, dense nuclear star formation may trap N-rich gas in proto-GCs; associated runaway stellar collisions could produce intermediate-mass black hole seeds, whose accretion is visible through their broad line region.

ACKNOWLEDGEMENTS

We thank S. Monty for having useful discussions of GCs. YI is supported by JSPS KAKENHI Grant No. 24KJ0202. RM, FDE, XJ, and JS acknowledge support by the Science and Technology Facilities Council (STFC), by the ERC through Advanced Grant 695671 “QUENCH”, and by the UKRI Frontier Research grant RISEand-FALL. RM also acknowledges funding from a research professorship from the Royal Society. IJ acknowledges support by the Huo Family Foundation through a P.C. Ho PhD Studentship. AF acknowledges the support from project “VLT- MOONS” CRAM 1.05.03.07, INAF Large Grant 2022 “The metal circle: a new sharp view of the baryon cycle up to Cosmic Dawn with the latest generation IFU facilities” and INAF Large Grant 2022 “Dual and binary SMBH in the multi-messenger era”. HÜ acknowledges funding by the European Union (ERC APEX, 101164796). Views and opinions expressed are however those of the authors only and do not necessarily reflect those of the European Union or the European Research Council Executive Agency. Neither the European Union nor the granting authority can be held responsible for them. AJB acknowledges funding from the “FirstGalaxies” Advanced Grant from the European Research Council (ERC) under the European Union’s Horizon 2020 research and innovation programme (Grant agreement No. 789056). SC acknowledges support by European Union’s HE ERC Starting Grant No. 101040227 - WINGS. ECL acknowledges support of an STFC Webb Fellowship (ST/W001438/1). BER acknowledges support from the NIRCAM Science Team contract to the University of Arizona, NAS5-02015, and JWST Program 3215. JW gratefully acknowledges support from the Cosmic Dawn Center through the DAWN Fellowship. The Cosmic Dawn Center (DAWN) is funded by the Danish National Research Foundation under grant No. 140. This work is based

on observations made with the NASA/ESA/CSA James Webb Space Telescope. The data were obtained from the Mikulski Archive for Space Telescopes at the Space Telescope Science Institute, which is operated by the Association of Universities for Research in Astronomy, Inc., under NASA contract NAS 5-03127 for JWST. These observations are associated with programmes #1180, 1181, 1210, 1286, 1287, and 3215. The authors acknowledge use of the lux supercomputer at UC Santa Cruz, funded by NSF MRI grant AST 1828315.

DATA AVAILABILITY

The bulk of the JWST/NIRSpec data used in this Letter are released by the JADES NIRSpec DR1 (Bunker et al. 2024) and DR3 (D'Eugenio et al. 2025), which are available on the JADES MAST website (<https://archive.stsci.edu/hlsp/jades>; MAST DOI: [10.17909/8tdj-8n28](https://doi.org/10.17909/8tdj-8n28)). The rest of datasets will also be public in the MAST archive. Our analysed data will be made available upon reasonable request.

REFERENCES

- Álvarez-Márquez J., et al., 2025, *A&A*, **695**, A250
- Alves de Oliveira C., et al., 2018, in *Observatory Operations: Strategies, Processes, and Systems VII*. p. 107040Q ([arXiv:1805.06922](https://arxiv.org/abs/1805.06922)), doi:[10.1117/12.2313839](https://doi.org/10.1117/12.2313839)
- Amorín R. O., Pérez-Montero E., Vílchez J. M., 2010, *ApJ*, **715**, L128
- Arellano-Córdova K. Z., et al., 2024, *arXiv e-prints*, p. [arXiv:2412.10557](https://arxiv.org/abs/2412.10557)
- Asplund M., Amarsi A. M., Grevesse N., 2021, *A&A*, **653**, A141
- Baldwin A., Phillips M. M., Terlevich R., 1981, *PASP*, **93**, 817
- Batra N. D., Baldwin J. A., 2014, *MNRAS*, **439**, 771
- Berg D. A., Skillman E. D., Henry R. B. C., Erb D. K., Carigi L., 2016, *ApJ*, **827**, 126
- Berg D. A., Erb D. K., Henry R. B. C., Skillman E. D., McQuinn K. B. W., 2019, *ApJ*, **874**, 93
- Böker T., et al., 2022, *A&A*, **661**, A82
- Bottorff M., Lamothe J., Momjian E., Verner E., Vinković D., Ferland G., 1998, *PASP*, **110**, 1040
- Bunker A. J., NIRSPEC Instrument Science Team JADESs Collaboration 2020, in da Cunha E., Hodge J., Afonso J., Pentericci L., Sobral D., eds, *IAU Symposium Vol. 352, Uncovering Early Galaxy Evolution in the ALMA and JWST Era*. pp 342–346 ([arXiv:2112.15207](https://arxiv.org/abs/2112.15207)), doi:[10.1017/S1743921319009463](https://doi.org/10.1017/S1743921319009463)
- Bunker A. J., et al., 2023, *A&A*, **677**, A88
- Bunker A. J., et al., 2024, *A&A*, **690**, A288
- Calzetti D., Armus L., Bohlin R. C., Kinney A. L., Koornneef J., Storchi-Bergmann T., 2000, *ApJ*, **533**, 682
- Cameron A. J., Katz H., Rey M. P., Saxena A., 2023a, *MNRAS*, **523**, 3516
- Cameron A. J., et al., 2023b, *A&A*, **677**, A115
- Cantiello M., Jermyn A. S., Lin D. N. C., 2021, *ApJ*, **910**, 94
- Carnall A. C., 2017, *arXiv e-prints*, p. [arXiv:1705.05165](https://arxiv.org/abs/1705.05165)
- Carretta E., Gratton R. G., Lucatello S., Bragaglia A., Bonifacio P., 2005, *A&A*, **433**, 597
- Castellano M., et al., 2024, *ApJ*, **972**, 143
- Charbonnel C., Schaerer D., Prantzos N., Ramírez-Galeano L., Fragos T., Kuruvanthodi A., Marques-Chaves R., Gieles M., 2023, *A&A*, **673**, L7
- Curti M., et al., 2024, *arXiv e-prints*, p. [arXiv:2407.02575](https://arxiv.org/abs/2407.02575)
- D'Antona F., et al., 2023, *A&A*, **680**, L19
- D'Eugenio F., et al., 2025, *ApJS*, **277**, 4
- Dall'Amico M., Mapelli M., Iorio G., Costa G., Charlot S., Korb E., Sgalietta C., Lecroq M., 2025, *A&A*, **695**, A221
- Dorner B., et al., 2016, *A&A*, **592**, A113
- Eisenstein D. J., et al., 2023a, *arXiv e-prints*, p. [arXiv:2306.02465](https://arxiv.org/abs/2306.02465)
- Eisenstein D. J., et al., 2023b, *arXiv e-prints*, p. [arXiv:2310.12340](https://arxiv.org/abs/2310.12340)
- Ferland G. J., et al., 2013, *Rev. Mex. Astron. Astrofis.*, **49**, 137
- Ferruit P., et al., 2022, *A&A*, **661**, A81
- Fukushima H., Yajima H., 2024, *PASJ*, **76**, 1122
- Gardner J. P., et al., 2023, *PASP*, **135**, 068001
- Garnett D. R., 1992, *AJ*, **103**, 1330
- Gieles M., et al., 2018, *MNRAS*, **478**, 2461
- Gordon K. D., Clayton G. C., Misselt K. A., Landolt A. U., Wolff M. J., 2003, *ApJ*, **594**, 279
- Häberle M., et al., 2024, *Nature*, **631**, 285
- Harikane Y., et al., 2023, *ApJ*, **959**, 39
- Harikane Y., et al., 2025, *ApJ*, **980**, 138
- Hayes M. J., Saldana-Lopez A., Citro A., James B. L., Mingozi M., Scarlata C., Martinez Z., Berg D. A., 2025, *ApJ*, **982**, 14
- Heard C. Z. P., Gaskell C. M., 2016, *MNRAS*, **461**, 4227
- Hirschmann M., et al., 2023, *MNRAS*, **526**, 3610
- Inayoshi K., Visbal E., Haiman Z., 2020, *ARA&A*, **58**, 27
- Inoguchi M., Hosokawa T., Fukushima H., Tanaka K. E. I., Yajima H., Mineshige S., 2024, *MNRAS*, **527**, 3612
- Isobe Y., et al., 2022, *ApJ*, **925**, 111
- Isobe Y., Ouchi M., Nakajima K., Harikane Y., Ono Y., Xu Y., Zhang Y., Umeda H., 2023a, *ApJ*, **956**, 139
- Isobe Y., et al., 2023b, *ApJ*, **959**, 100
- Izotov Y. I., Stasińska G., Meynet G., Guseva N. G., Thuan T. X., 2006, *A&A*, **448**, 955
- Jakobsen P., et al., 2022, *A&A*, **661**, A80
- Ji X., et al., 2024, *MNRAS*, **535**, 881
- Juodžbalis I., et al., 2024, *Nature*, **636**, 594
- Juodžbalis I., et al., 2025, *arXiv e-prints*, p. [arXiv:2504.03551](https://arxiv.org/abs/2504.03551)
- Kobayashi C., Ferrara A., 2024, *ApJ*, **962**, L6
- Kocevski D. D., et al., 2023, *ApJ*, **954**, L4
- Kojima T., et al., 2020, *ApJ*, **898**, 142
- Kumari N., James B. L., Irwin M. J., Amorín R., Pérez-Montero E., 2018, *MNRAS*, **476**, 3793
- Lambrides E., et al., 2024, *arXiv e-prints*, p. [arXiv:2409.13047](https://arxiv.org/abs/2409.13047)
- Larson R. L., et al., 2023, *ApJ*, **953**, L29
- Lennox D. J., Burke V. M., 1994, *A&AS*, **103**, 273
- Li S., et al., 2025, *ApJ*, **979**, L13
- Luridiana V., Morisset C., Shaw R. A., 2015, *A&A*, **573**, A42
- Maiolino R., et al., 2024a, *Nature*, **627**, 59
- Maiolino R., et al., 2024b, *A&A*, **691**, A145
- Marques-Chaves R., et al., 2024, *A&A*, **681**, A30
- Mazzolari G., et al., 2024, *A&A*, **691**, A345
- Nagele C., Umeda H., 2023, *ApJ*, **949**, L16
- Nandal D., Regan J. A., Woods T. E., Farrell E., Ekström S., Meynet G., 2024, *A&A*, **683**, A156
- Napolitano L., et al., 2024, *arXiv e-prints*, p. [arXiv:2410.18763](https://arxiv.org/abs/2410.18763)
- Navarro-Carrera R., Caputi K. I., Iani E., Rinaldi P., Kokorev V., Kerutt J., 2024, *arXiv e-prints*, p. [arXiv:2407.14201](https://arxiv.org/abs/2407.14201)
- Nicholls D. C., Sutherland R. S., Dopita M. A., Kewley L. J., Groves B. A., 2017, *MNRAS*, **466**, 4403
- Partmann C., Naab T., Lahén N., Rantala A., Hirschmann M., Hislop J. M., Petersson J., Johansson P. H., 2025, *MNRAS*, **537**, 956
- Pascale M., Dai L., McKee C. F., Tsang B. T. H., 2023, *ApJ*, **957**, 77
- Rantala A., Naab T., Lahén N., 2024a, *MNRAS*, **531**, 3770
- Rantala A., Rawlings A., Naab T., Thomas J., Johansson P. H., 2024b, *MNRAS*, **535**, 1202
- Reddy N. A., Topping M. W., Sanders R. L., Shapley A. E., Brammer G., 2023a, *ApJ*, **948**, 83
- Reddy N. A., Topping M. W., Sanders R. L., Shapley A. E., Brammer G., 2023b, *ApJ*, **952**, 167
- Renzini A., 2023, *MNRAS*, **525**, L117
- Rieke M., 2020, in da Cunha E., Hodge J., Afonso J., Pentericci L., Sobral D., eds, *IAU Symposium Vol. 352, Uncovering Early Galaxy Evolution in the ALMA and JWST Era*. pp 337–341, doi:[10.1017/S1743921319008950](https://doi.org/10.1017/S1743921319008950)
- Rigby J., et al., 2023, *PASP*, **135**, 048001
- Rizzuti F., Matteucci F., Molaro P., Cescutti G., Maiolino R., 2024, *arXiv e-prints*, p. [arXiv:2412.05363](https://arxiv.org/abs/2412.05363)
- Sakurai Y., Yoshida N., Fujii M. S., 2019, *MNRAS*, **484**, 4665

- Salpeter E. E., 1955, [ApJ](#), **121**, 161
- Sandles L., et al., 2024, [A&A](#), **691**, A305
- Schaerer D., Marques-Chaves R., Xiao M., Korber D., 2024, [A&A](#), **687**, L11
- Scholtz J., et al., 2023, [arXiv e-prints](#), p. [arXiv:2311.18731](#)
- Senchyna P., Plat A., Stark D. P., Rudie G. C., Berg D., Charlot S., James B. L., Mingozi M., 2024, [ApJ](#), **966**, 92
- Stanway E. R., Eldridge J. J., 2018, [MNRAS](#), **479**, 75
- Steidel C. C., Strom A. L., Pettini M., Rudie G. C., Reddy N. A., Trainor R. F., 2016, [ApJ](#), **826**, 159
- Stiavelli M., et al., 2025, [ApJ](#), **981**, 136
- Taylor A. J., et al., 2024, [arXiv e-prints](#), p. [arXiv:2409.06772](#)
- Telles E., Thuan T. X., Izotov Y. I., Carrasco E. R., 2014, [A&A](#), **561**, A64
- Temple M. J., Ferland G. J., Rankine A. L., Chatzikos M., Hewett P. C., 2021, [MNRAS](#), **505**, 3247
- Topping M. W., et al., 2024, [MNRAS](#), **529**, 3301
- Topping M. W., et al., 2025, [ApJ](#), **980**, 225
- Trinca A., et al., 2024, [arXiv e-prints](#), p. [arXiv:2412.14248](#)
- Tripodi R., et al., 2024, [arXiv e-prints](#), p. [arXiv:2412.04983](#)
- Übler H., et al., 2023, [A&A](#), **677**, A145
- Veilleux S., Osterbrock D. E., 1987, [ApJS](#), **63**, 295
- Vincenzo F., Belfiore F., Maiolino R., Matteucci F., Ventura P., 2016, [MNRAS](#), **458**, 3466
- Vink J. S., 2023, [A&A](#), **679**, L9
- Watanabe K., et al., 2024, [ApJ](#), **962**, 50
- Yanagisawa H., et al., 2024, [ApJ](#), **974**, 266
- Zhang Y., Morishita T., Stiavelli M., 2025, [arXiv e-prints](#), p. [arXiv:2502.04817](#)
- de Graaff A., et al., 2024, [A&A](#), **684**, A87

This paper has been typeset from a $\mathrm{T}_{\mathrm{E}}\mathrm{X}/\mathrm{L}^{\mathrm{A}}\mathrm{T}_{\mathrm{E}}\mathrm{X}$ file prepared by the author.